Supplementary Materials for Understanding the Conversion Mechanism of Transition Metal Fluoride Cathodes: the Case of Monodisperse CoF_2 Nanocrystals

Liwei Dai[1], Kevin C. Matthews[2], Albert Xiao[1], Johannes Ihli[1], Taewon Kim[1], Jamie Warner[2], Mauro Pasta[1*]

[*]Corresponding author. Email: mauro.pasta@materials.ox.ac.uk

This PDF file includes:

Supplementary Text

Figures S1 to S21

Supplementary Text

Li elemental map processing

The quantification of Li in the CoF_2 samples was performed using a modified S_A/S_B method, developed based on the approach by Kikkawa *et al.* (*57*).

Between the spectra measured from the lithiated and un-lithiated regions, a notable difference is observed in the Li K and Co $M_{2,3}$ edges: a second peak appears in the lithiated region compared to the un-lithiated region (Figure S20 (a)-(c)). More specifically, spectra measured from un-lithiated, partially-lithiated, and fully-lithiated regions reveal that the peak intensities in the 68-72 eV energy loss range become progressively more prominent as the lithiation increases, while the tail in the 74-80 eV range remains unchanged. This suggests that the rise in the second peak feature is predominantly due to the presence of Li.

Thus, the Li elemental map can be generated by accurately quantifying the rise in this second peak within the 68-72 eV range attributed only to the presence of Li K edge (S_A), while assuming the contribution from the Co $M_{2,3}$ edges (S_B) remains relatively constant whether the Li K edge is present or not. To quantify this, an approximation of the "constant" Co $M_{2,3}$ edge is required. This is achieved by approximating the Co $M_{2,3}$ edge by extrapolating a "baseline" as the extension of the descending tail in the reverse direction. Specifically, this "baseline" is created by performing a power-law fitting to the unprocessed edge tail over the 74-80 eV fitting window (δ_B), and extrapolating it back towards the lower energy loss direction. In the un-lithiated region, where the spectrum consists solely of Co $M_{2,3}$ edges, this fitting closely matches the 68-72 eV range, demonstrating the feasibility of the approximation (Figure S20 (a)).

As illustrated in Figure S20 (a)-(c), a power-law baseline is created from the fitting window (δ_C). The area between the unprocessed spectrum and the fitted Co $M_{2,3}$ edge within the 68-72 eV range is marked as S_A, representing the additional signals from the Li K edge. The area between the Co $M_{2,3}$ fit and the power-law baseline (created from the fitting window δ_C) within the same energy loss range is marked as S_B. Thus, the S_A/S_B is a representation of the Li concentration based on a relatively constant Co concentration. It is important to note that the S_A/S_B method does not fully isolate the Li K edge from the Co $M_{2,3}$ edges, as the rising tail of the Co $M_{2,3}$ edges may include some contribution from the Li K edge. Although the complete separation between the Li K

edge and the Co $M_{2,3}$ edges is not achieved by this method, the S_A/S_B value should still be a good representation of the relative Li concentration, which can be used to map the spatial distribution and concentration of Li elements in the sample.

This interpretation is further supported by overlapping the Li map with Co and F elemental maps (Figure S21). A strong correlation between these elements in the converted region (top-right) is observed, with Li-rich areas (red pixels) are found in between Co-rich regions (green pixels), consistent with the formation of spatially separated LiF and Co phases. This confirms that the Li signals represent true high-resolution features rather than noise, highlighting the accuracy and effectiveness of the S_A/S_B method in mapping the Li distribution and concentration.

Supplementary Figures

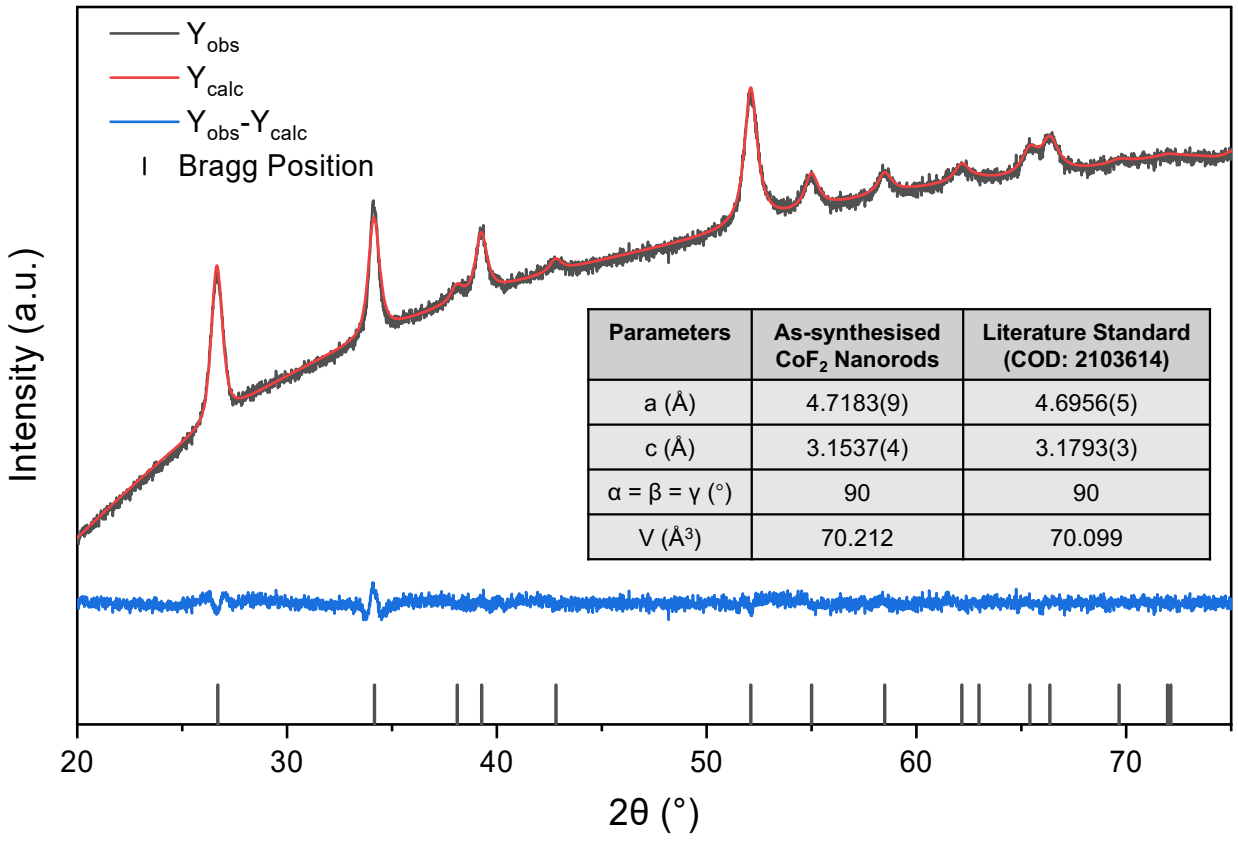

Parameters	As-synthesised CoF_2 Nanorods	Literature Standard (COD: 2103614)
a (Å)	4.7183(9)	4.6956(5)
c (Å)	3.1537(4)	3.1793(3)
α = β = γ (°)	90	90
V (Å³)	70.212	70.099

Figure S1: XRD Analysis of As-synthesised CoF_2 Nanorods. Rietveld refinement of XRD patterns measured from the as-synthesised CoF_2 sample showing the calculated lattice parameters. The calculated lattice parameters match with the literature standard (COD ID: 2103614) (*49*).

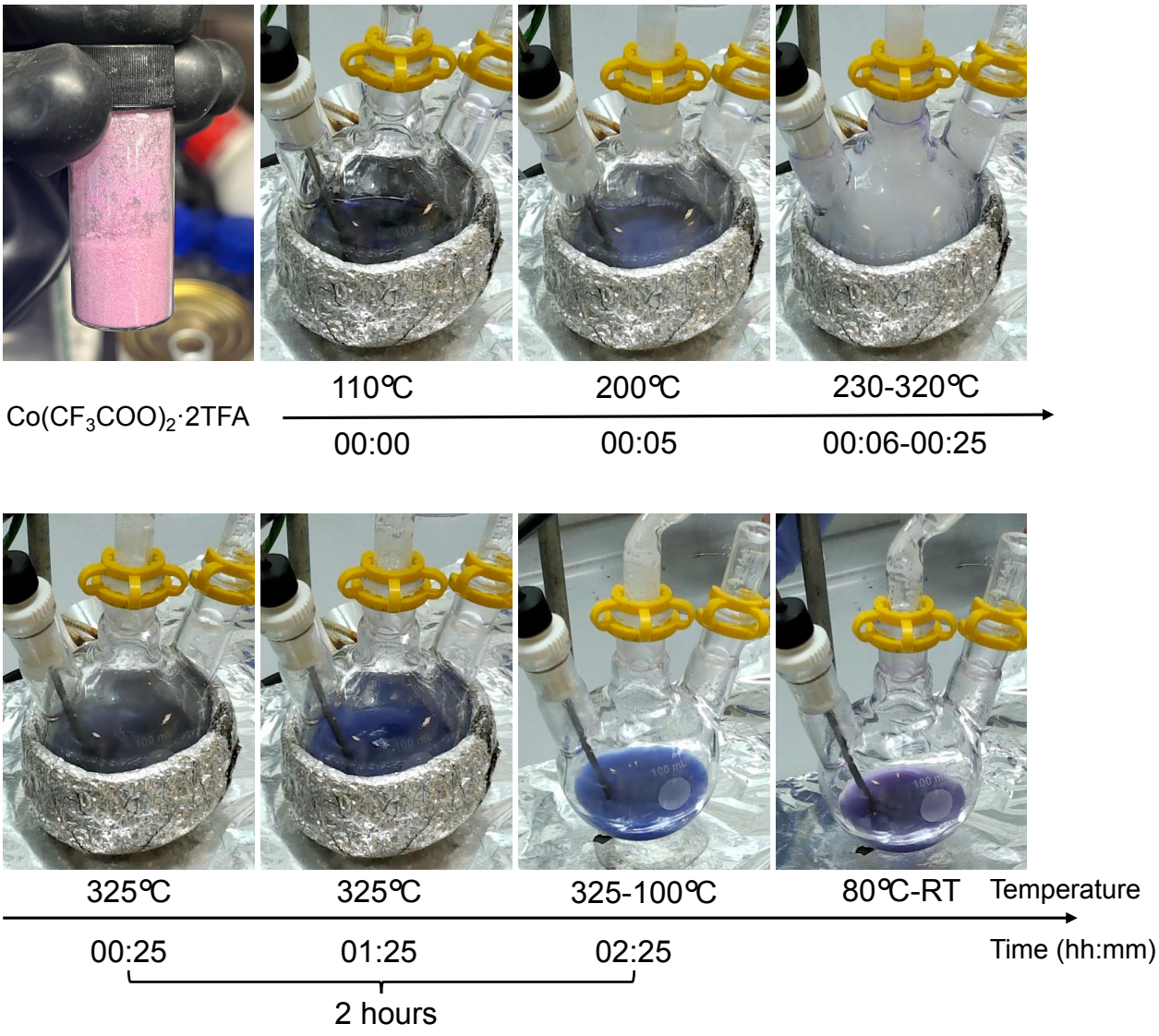

Figure S2: Photographs of the $Co(CF_3COO)_2 \cdot 2TFA$ precursor and the reaction dynamics of the colloidal synthesis over time and temperature.

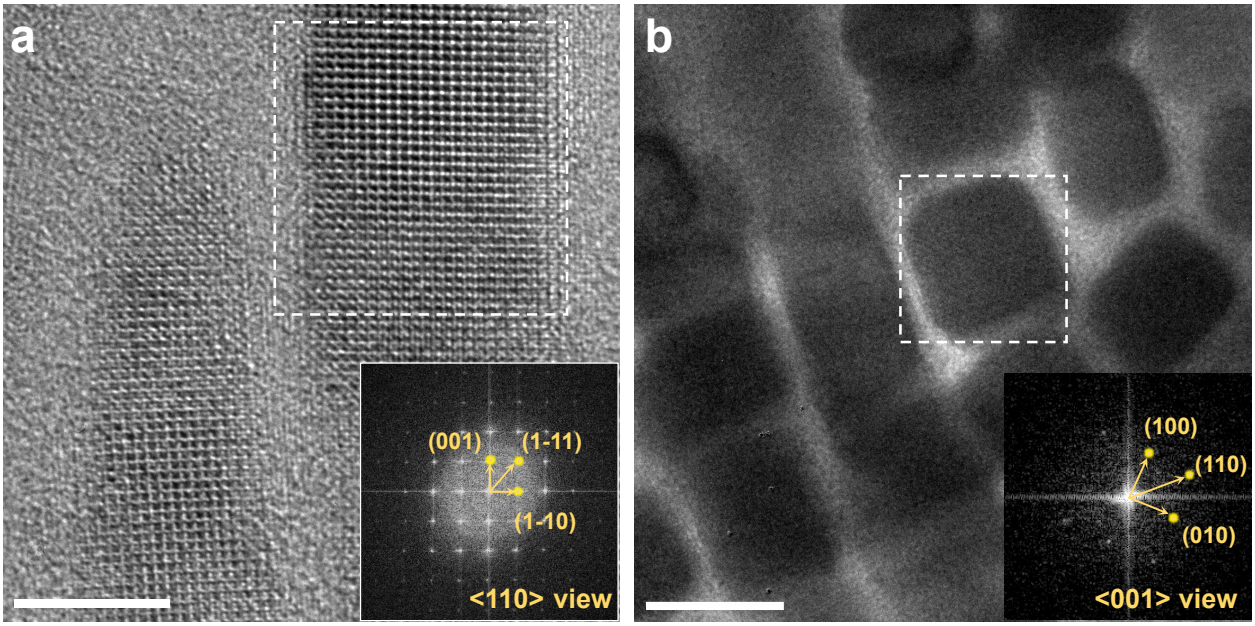

Figure S3: TEM Images of CoF_2 Nanorods from Side and Top/bottom Views. **(a)** CoF_2 nanorods side view at $\langle 110 \rangle$ zone axis. **(b)** CoF_2 nanorods top/bottom view at $\langle 001 \rangle$ zone axis. Although most of the drop-casted nanorods naturally align on their side planes, some are randomly oriented on their top/bottom planes, providing both side and top/bottom views. Insets are the FFT patterns taken from regions indicated by white dashed boxes in each TEM image. Scale bar = 5 nm in **(a)**; 10 nm in **(b)**.

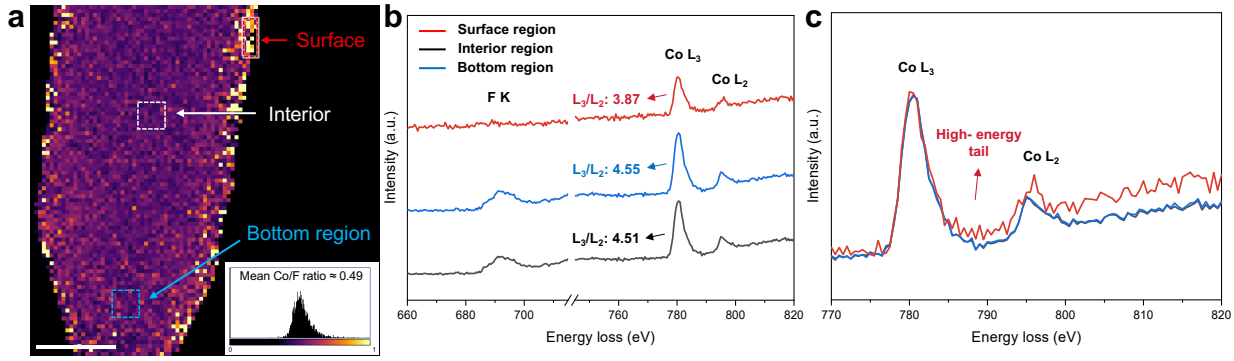

Figure S4: Stage 1: Surface Li^+ Insertion. (**a**) Elemental maps of Co/F measured at point **C**, showing the formation of a Co-rich layer at nanorod surface. The Co and F signals remain homogeneously distributed at the interior and bottom regions. (**b**) Comparison of the core-loss EELS spectra measured from the nanorod surface, bottom-end and interior regions. Metallic Co at nanorod surface is indicated by the lower Co L_3/L_2 ratio and the absence of the F K edge. (**c**) Comparison of Co $L_{2,3}$ edges measured from the surface, bottom, and interior regions. All spectra were shifted and normalised to match the Co L_3 maximum peak position and intensity. Scale bars = 10 nm.

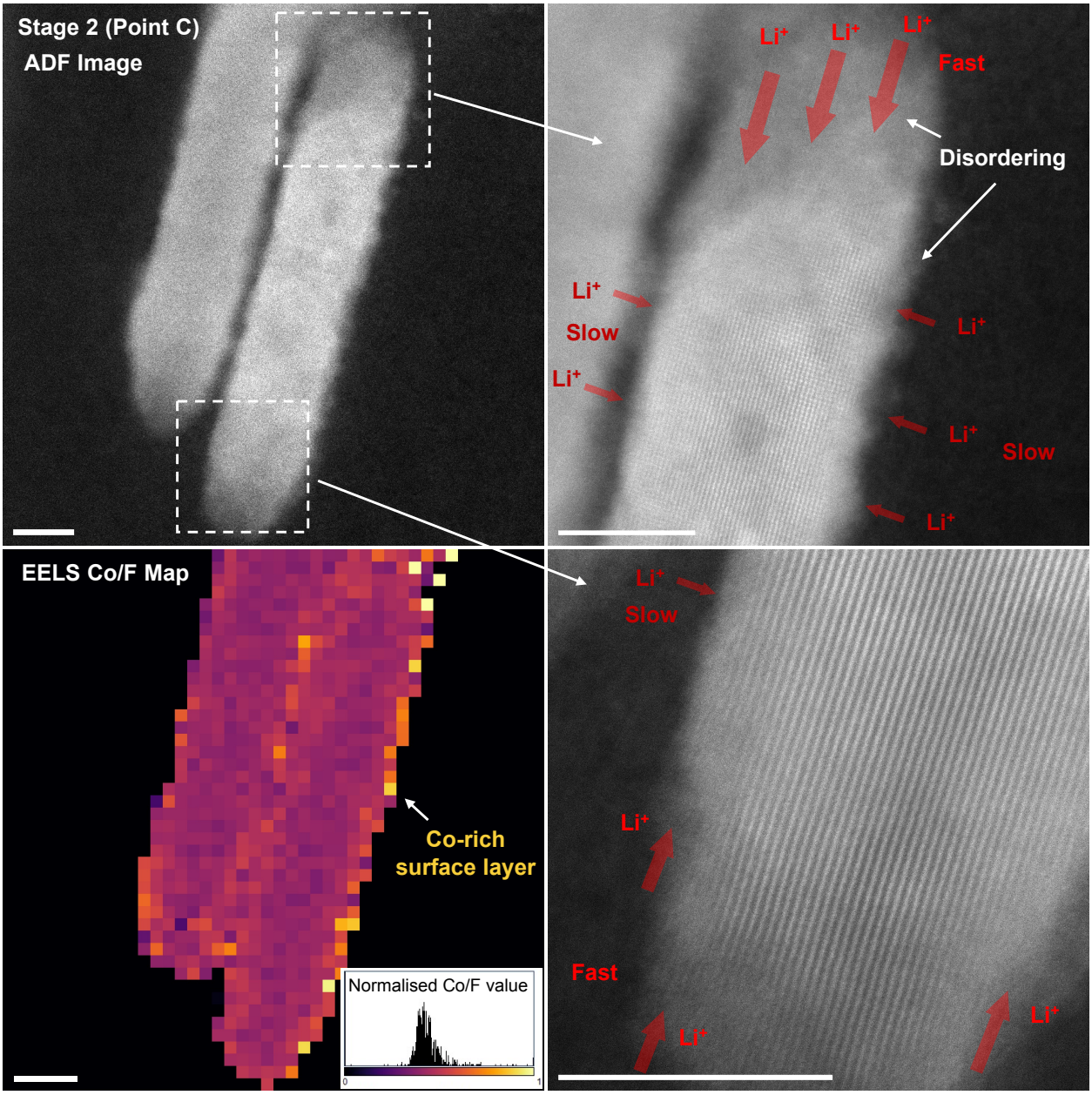

Figure S5: Stage 2: Interior Li^+ Insertion. Further Li^+ insertion occurs primarily through the $[001]_{CoF_2}$ channels from the top and bottom ends of the nanorod, causing structural disordering of the CoF_2 lattice in these regions. In contrast, Li^+ insertion through the $[110]_{CoF_2}$ channels encounters a significant energy barrier, resulting in the formation of a thin amorphous surface layer (1-2 nm). The EELS elemental Co/F map reveals that this disordered surface layer is Co-rich, while the Co and F signals remain homogeneously distributed in the disordered regions at the top and bottom ends and within the nanorod interior, maintaining a Co/F ratio of approximately 0.5. Scale bars = 10 nm for all images.

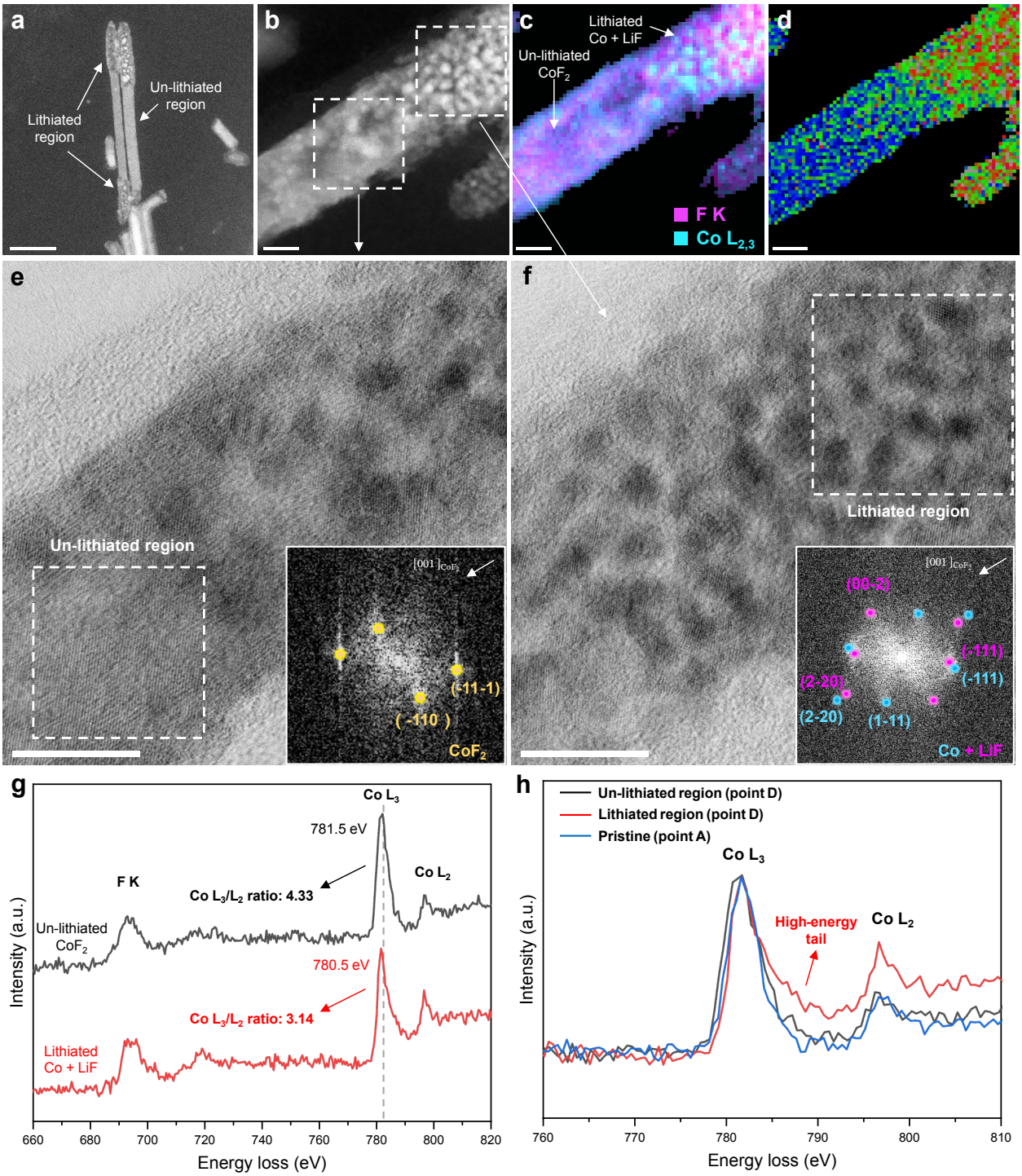

Figure S6: Stage 3 (Point D): Partial Conversion to Co Nanoparticles and LiF. (**a**) ADF image of nanorods at point **D**, illustrating lithiation occurs simultaneously from the {001} planes at both the top and bottom ends with significant volume expansion. (**b**)-(**d**) is a comparison between (**b**) the ADF image, (**c**) the overlay of Co and F elemental maps, and (**d**) the elemental map of Li, all obtained from the same region, visualising the spatial distribution of these elements. High magnification ABF images (**e**) and (**f**) were taken from the white boxes in (**a**), respectively. Insets show the FFT patterns derived from the un-lithiated and lithiated regions in the corresponding ABF images. (**g**) Comparison of the core-loss EELS spectra measured from the un-lithiated and lithiated regions. (**h**) Comparison of the Co $L_{2,3}$ edges measured from the un-lithiated and lithiated regions of sample **D** with pristine sample **A**. All spectra were shifted and normalised to match the Co L_3 maximum peak position and intensity. Scale bars = 50 nm in (**a**); 10 nm in (**b**)-(**f**).

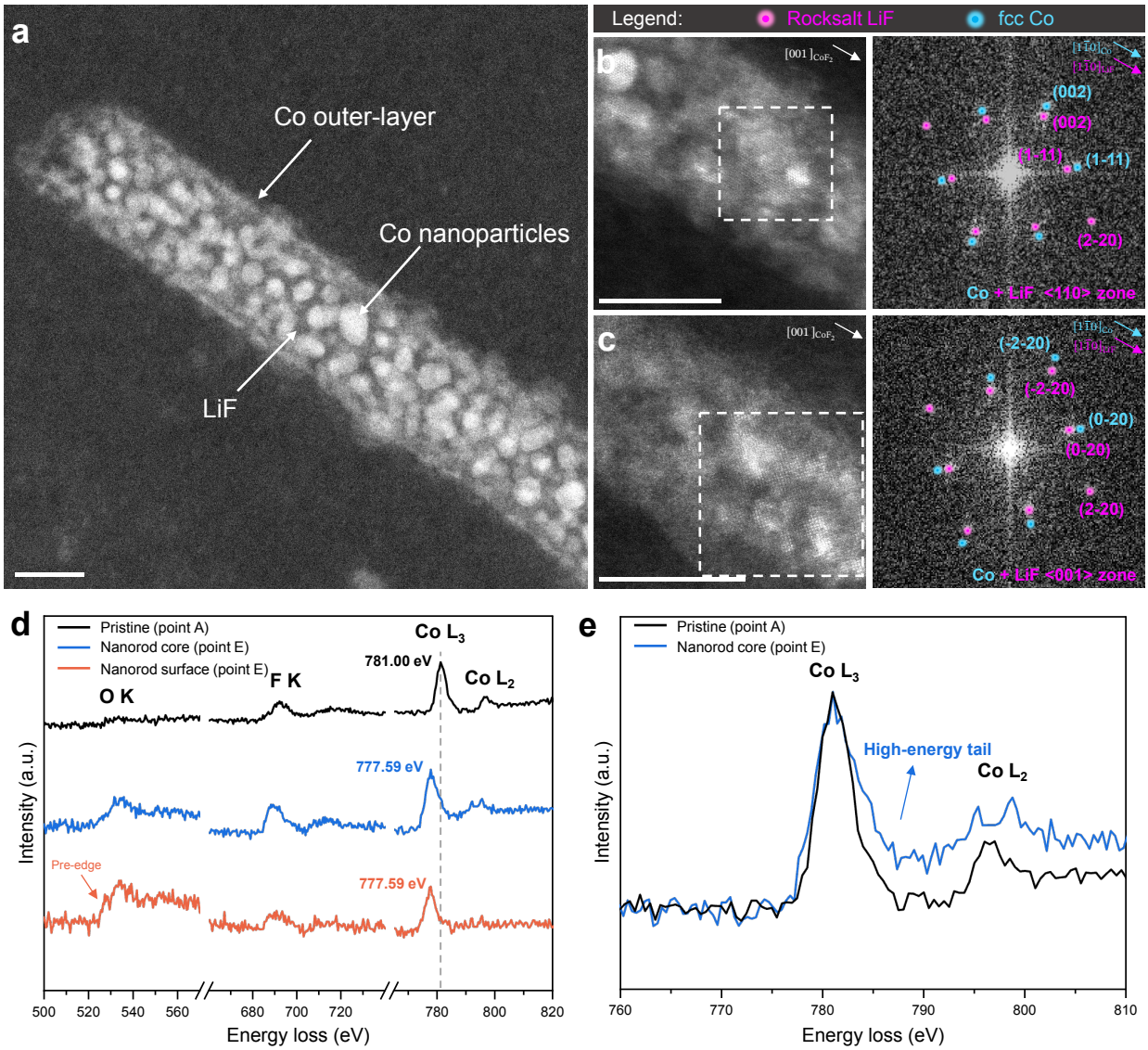

Figure S7: STEM ADF image of sample **E** (fully discharged state) in low magnification (**a**), showing the nucleation of cobalt nanoparticles within LiF matrix. STEM ADF images of sample **E** in high magnification with corresponding FFTs demonstrating orientation relationship between fcc-Co and LiF in (**b**) <110>view and (**c**) <001>view. [1-10] directions of LiF and fcc-Co remain parallel to the [001] direction of CoF_2. (**d**) Comparison of core-loss EELS spectra measured from the surface and interior region of sample **E**, and from pristine sample **A**. (**e**) Comparison of Co $L_{2,3}$ edges measured from sample **A** (pristine) and sample **E** (fully discharged state). All spectra were shifted and normalised to match the Co L_3 maximum peak position and intensity. Scale bars = 10 nm.

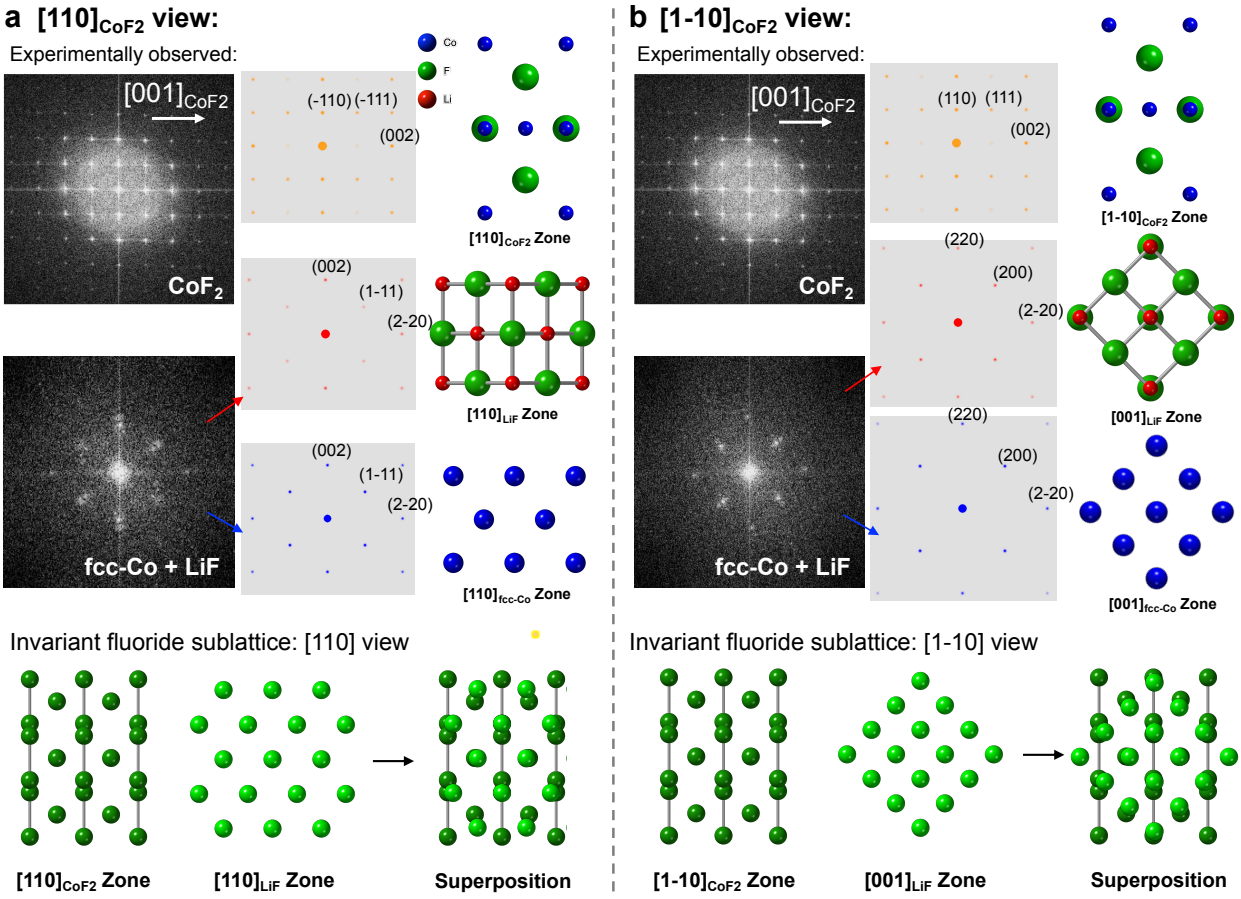

Figure S8: Orientation Relationship between CoF_2, LiF and fcc-Co. Comparison between the experimentally observed FFT patterns, computed diffraction patterns and the corresponding crystal structures from (**a**) $\langle 110 \rangle_{CoF_2}$ view and (**b**) $\langle 1\text{-}10 \rangle_{CoF_2}$ view. Bottom figures: crystal models of the fluoride sublattice in CoF_2 and LiF illustrate how the common fluoride lattice is preserved during the phase transformation from parent rutile CoF_2 to rocksalt LiF. The fluoride sublattice of LiF is highlighted in brighter green, demonstrating the topotactic relationship between the phases in the superposition view. A comparison is made between the crystal structures in both orientations, illustrating the remarkable similarity between their fluoride sublattices.

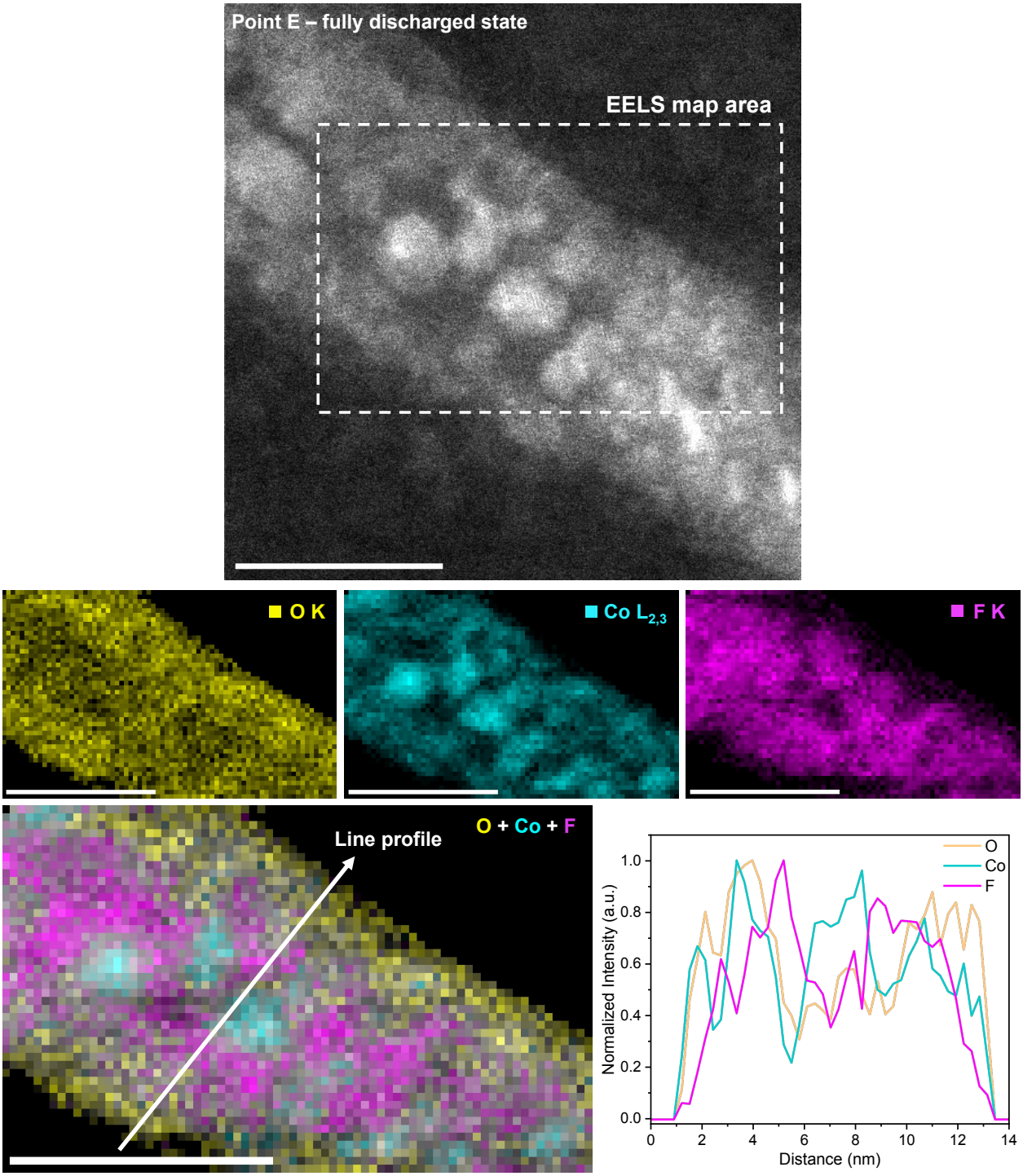

Figure S9: EELS Mapping of the Fully Discharged Nanorod. Top: the ADF image of a CoF_2 nanorod at the fully discharged state (point **E**). Middle: the oxygen K map, cobalt L map, and F K map derived from the mapping area. Bottom: Superposition of the O, Co, F maps and a line profile indicating the location of each element. Scale bars = 10 nm.

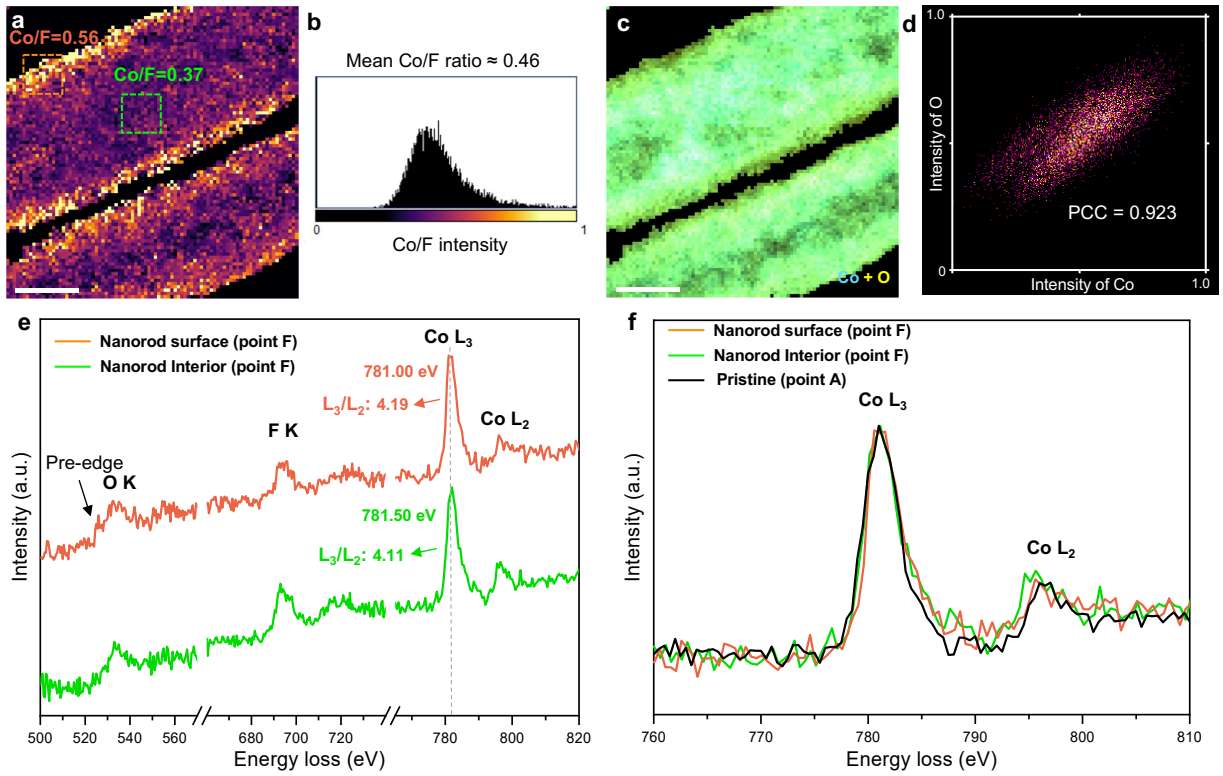

Figure S10: Stage 4: Interior Reconversion. (**a**) EELS elemental maps of Co/F, illustrating the Co-rich surface and the merging of Co and F signals within the nanorod interior. (**b**) Normalised histogram showing the relative Co/F ratios derived from the data in (**a**). **(c, d)** Colocalisation analysis reveals a positive linear correlation between Co and O signals at the nanorod surface. (**e**) Comparison of the core-loss EELS spectra measured from the nanorod interior and surface regions, demonstrating that the Co $L_{2,3}$ edges in both regions have shifted back to approximately 781.5 eV. (**f**) Comparison of the Co $L_{2,3}$ edges measured from the nanorod interior and surface of sample **F** with pristine sample **A**. All spectra were shifted and normalised to match the Co L_3 maximum peak position and intensity. Scale bars = 10 nm.

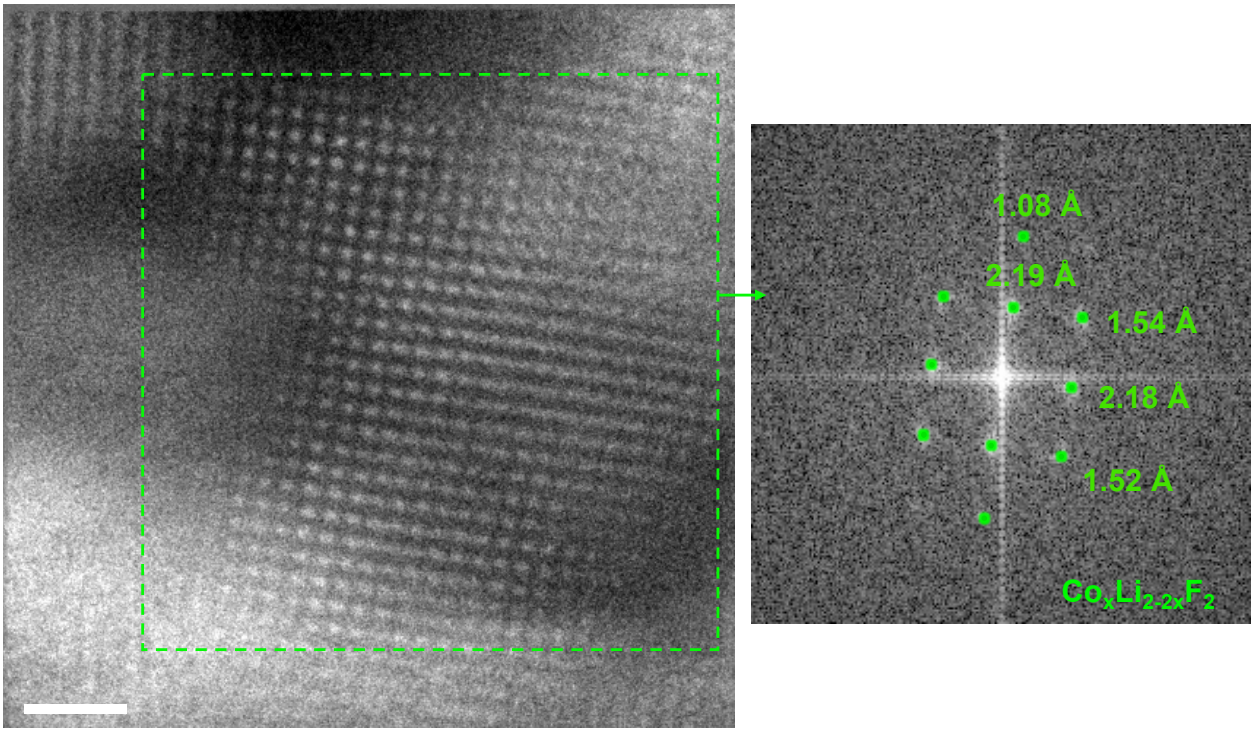

Figure S11: Stage 4: Formation of Intermediate Phase. High-magnification ADF image of a nanorod at point **F**, showing the crystal lattice corresponding to the rocksalt ⟨001⟩ zone axis. The corresponding FFT patterns derived from the region enclosed by the green box, revealing the merging of Co and LiF into a single rocksalt intermediate phase with slightly larger d-spacings to LiF. The lattice structure and orientation of this phase are identical to those of fcc-Co and rocksalt LiF, as viewed along the ⟨001⟩ zone axis. Scale bars = 10 nm.

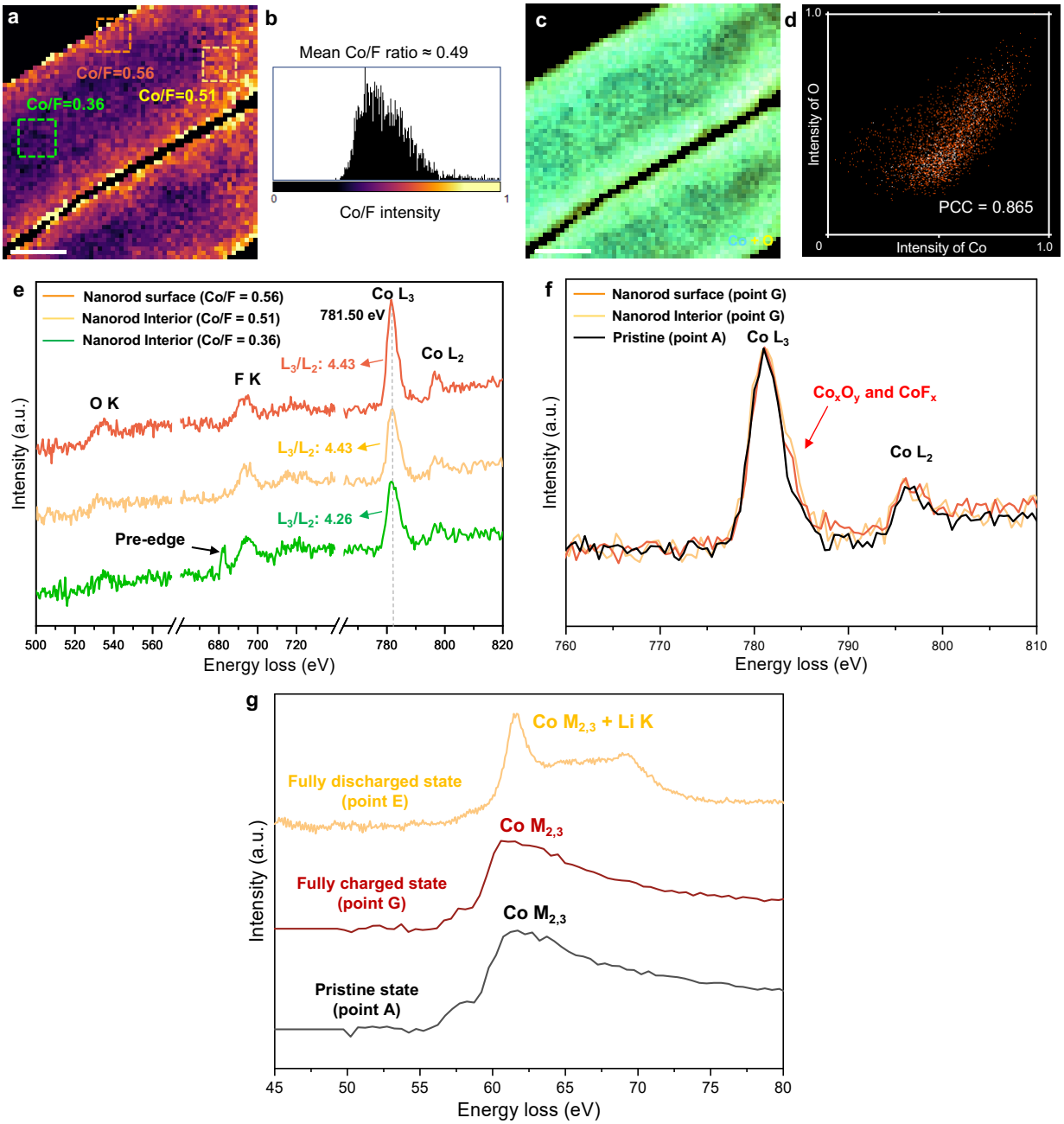

Figure S12: Stage 5: Surface Reconversion. (**a**) EELS elemental maps of Co/F, illustrating the thinning of the Co-rich surface layer and the gradual increase in the Co/F ratio from the nanorod surface to the interior. (**b**) Normalised histogram showing the relative Co/F ratios derived from the data in (**a**). An average Co/F ratio of approximately 0.5 indicates the preservation of Co and F elements in the nanorod. (**c, d**) Colocalisation analysis reveals a positive linear correlation between Co and O signals at the nanorod surface. (**e**) Comparison of core-loss EELS spectra measured from the surface and interior regions of sample **G**, demonstrating that the Co $L_{2,3}$ edges in all regions have shifted back to 781.5 eV. (**f**) Comparison of the Co $L_{2,3}$ edges measured from the interior and surface region of sample **G** with pristine sample **A**. All spectra were shifted and normalised to match the Co L_3 maximum peak position and intensity. (**g**) Comparison of the low-loss EELS spectra measured from sample **E** (fully discharged state), sample **G** (fully charged state), and sample **A** (pristine state). The absence of the Li K edge and the identical edge shapes between the spectra from sample **G** and sample **A** indicate the complete delithiation upon charging to 4.3 V vs. Li^+/Li. Scale bars = 10 nm.

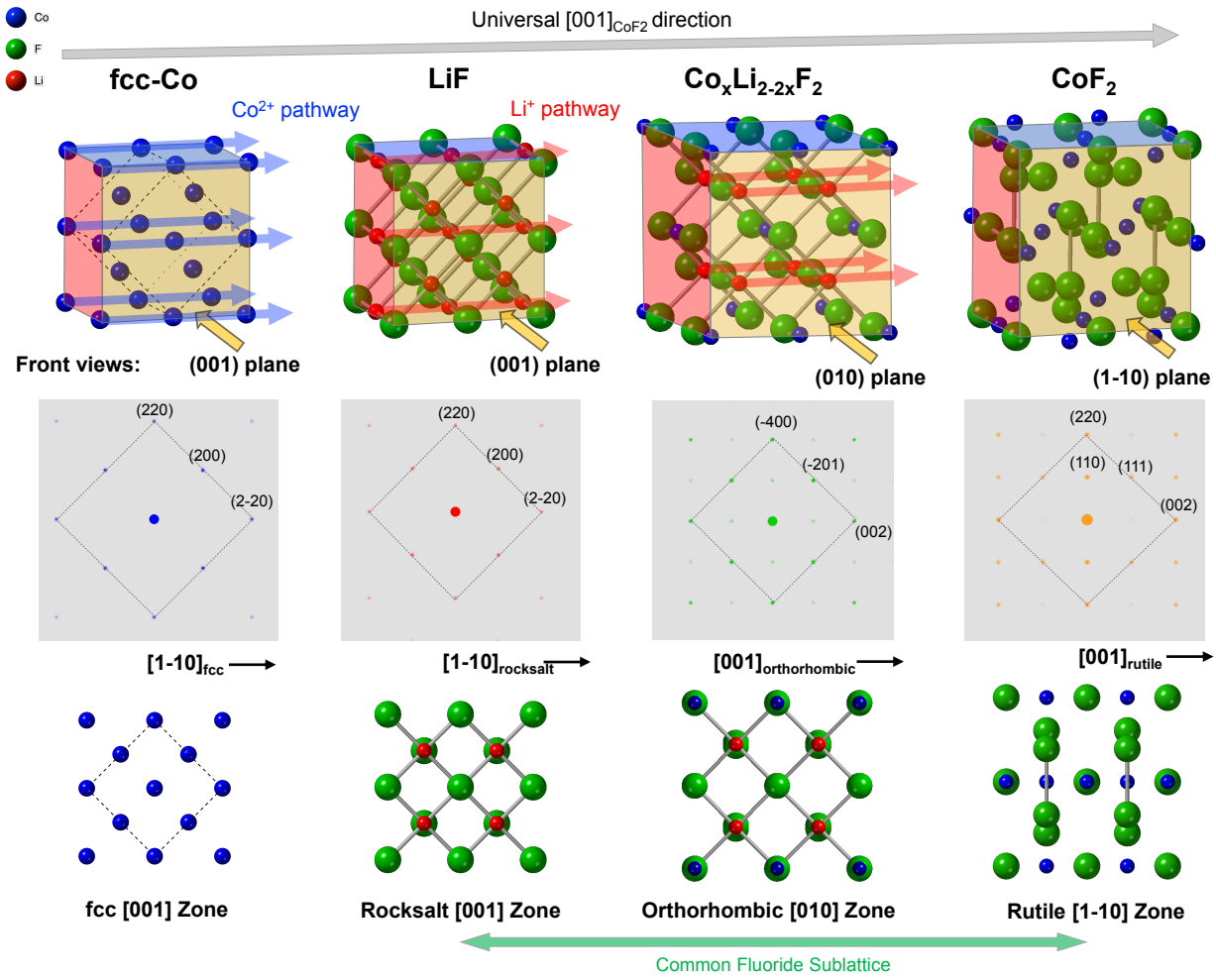

Figure S13: Topotactic Phase Transformations By the Preservation of A Common Fluoride Sublattice. Topotactic transformation between fcc, rocksalt, orthorhombic, and rutile structures, along the universal $[001]_{CoF_2}$ direction. Their crystal structures viewed from the $\langle 1\text{-}10\rangle_{CoF_2}$ zone axis are illustrated here. A highly topotactic relationship is found between this specific orientation relationship between all phases. The preservation of a common fluoride sublattice is demonstrated.

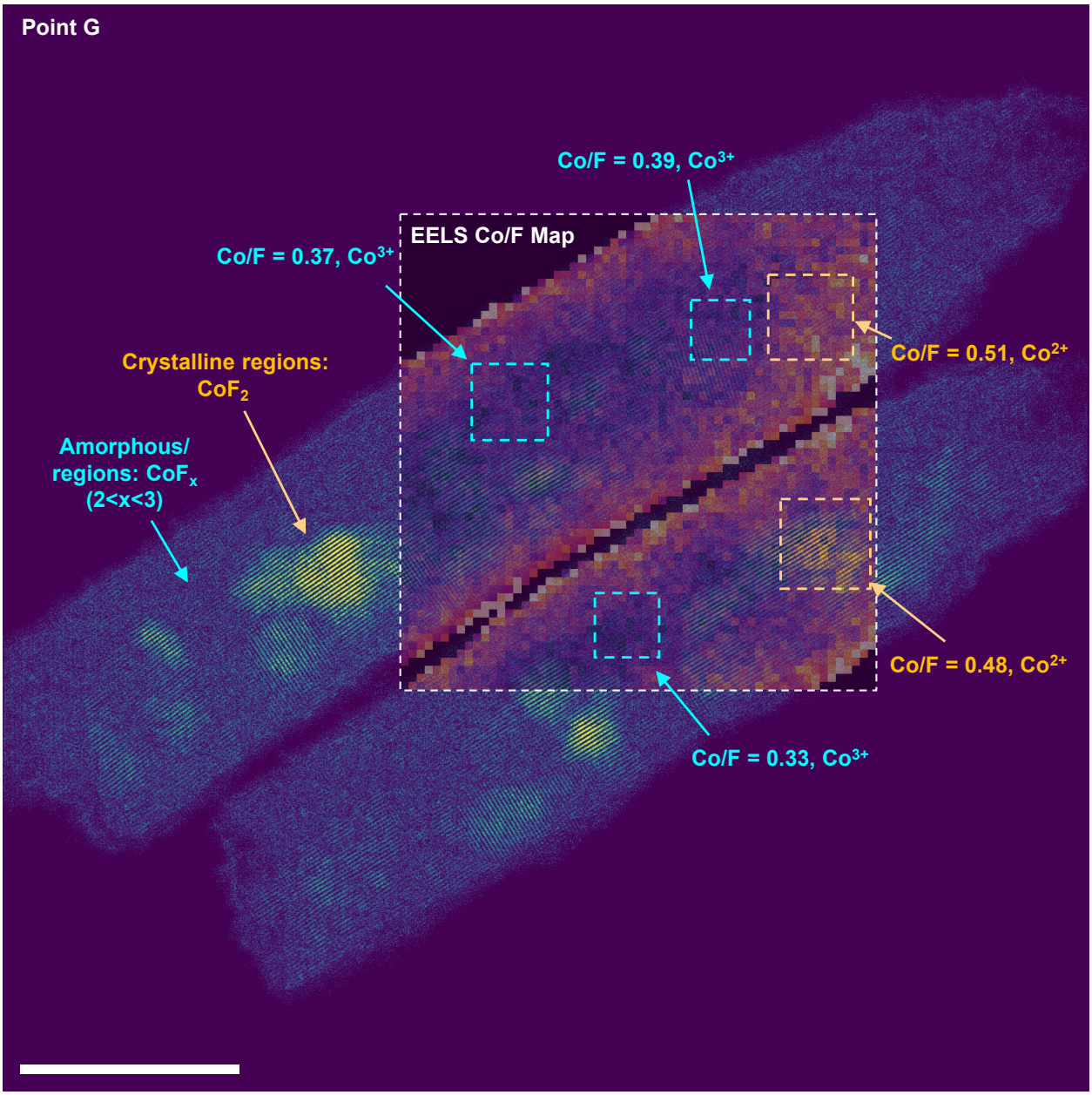

Figure S14: Stage 5: Incomplete Reconversion. ADF images of a fully charged nanorod at point **G**, partially overlapped with the Co/F elemental map from the EELS measurement. In the ADF image, the regions enclosed by yellow boxes highlight areas where crystalline rutile CoF_2 has reformed in small domains, corresponding to regions with a Co/F ratio around 0.5. The blue boxes indicate domains with a Co/F ratio of less than 0.5, where the structure is more disordered. In these regions, the presence of a pre-peak in the F K edge suggests the over-oxidation of Co to the 3+ oxidation state. Scale bars = 20 nm.

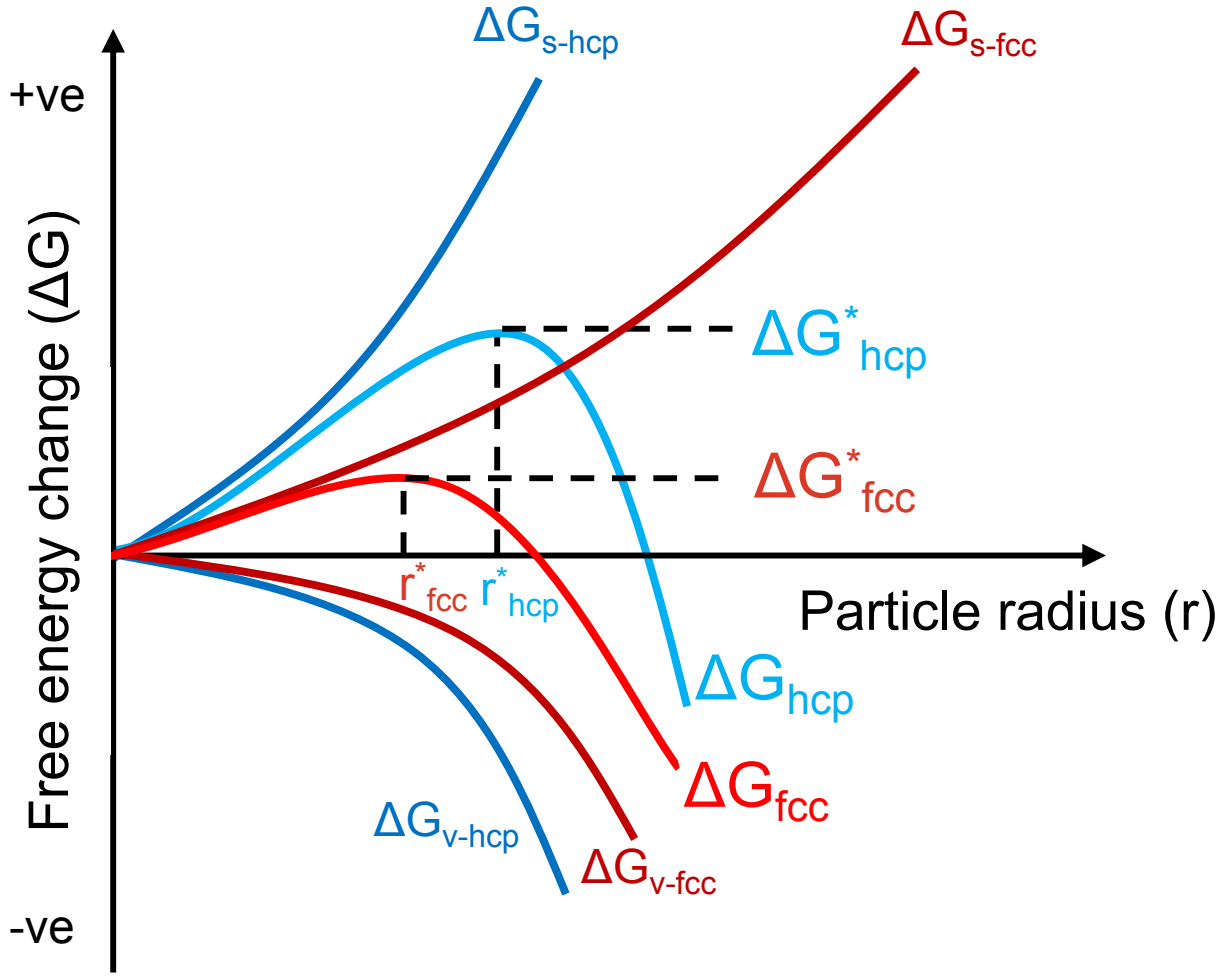

Figure S15: Free Energy Diagram of Co Nucleation in the fcc and hcp Phase. The free energy changes associated with the nucleation of fcc-Co and hcp-Co are denoted by red and blue curves, respectively. The fcc-Co curve (red) represents a smaller nucleation barrier and a smaller critical nucleus size due to its lower interfacial energy. The hcp-Co curve (blue) represents a higher nucleation barrier and a larger critical nucleus size due to its higher interfacial energy.

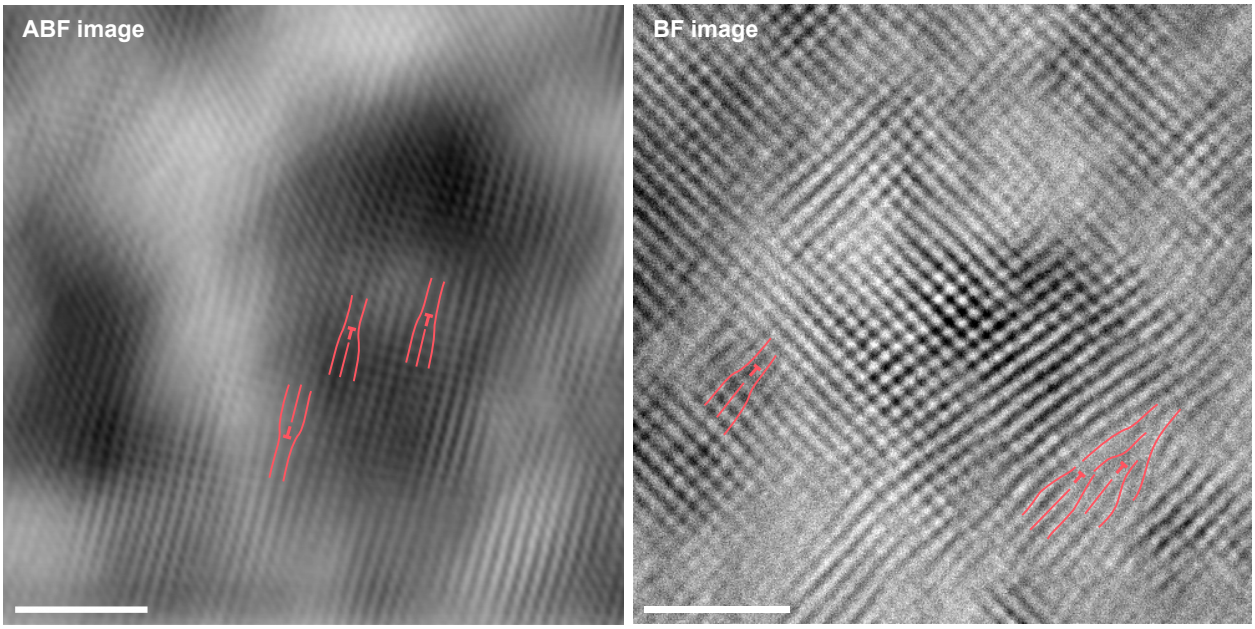

Figure S16: Dislocations at Interfaces Between fcc-Co and Rocksalt LiF. Misfit dislocations formed at the fcc-Co/LiF interfaces to relieve the strain caused by the lattice mismatching between two phases. The dislocations are denoted by red lines. The left ABF image is processed by using a threshold Fourier filter to enhance the SNR, improving clarity in visualising the lattice structures. Scale bar = 2 nm.

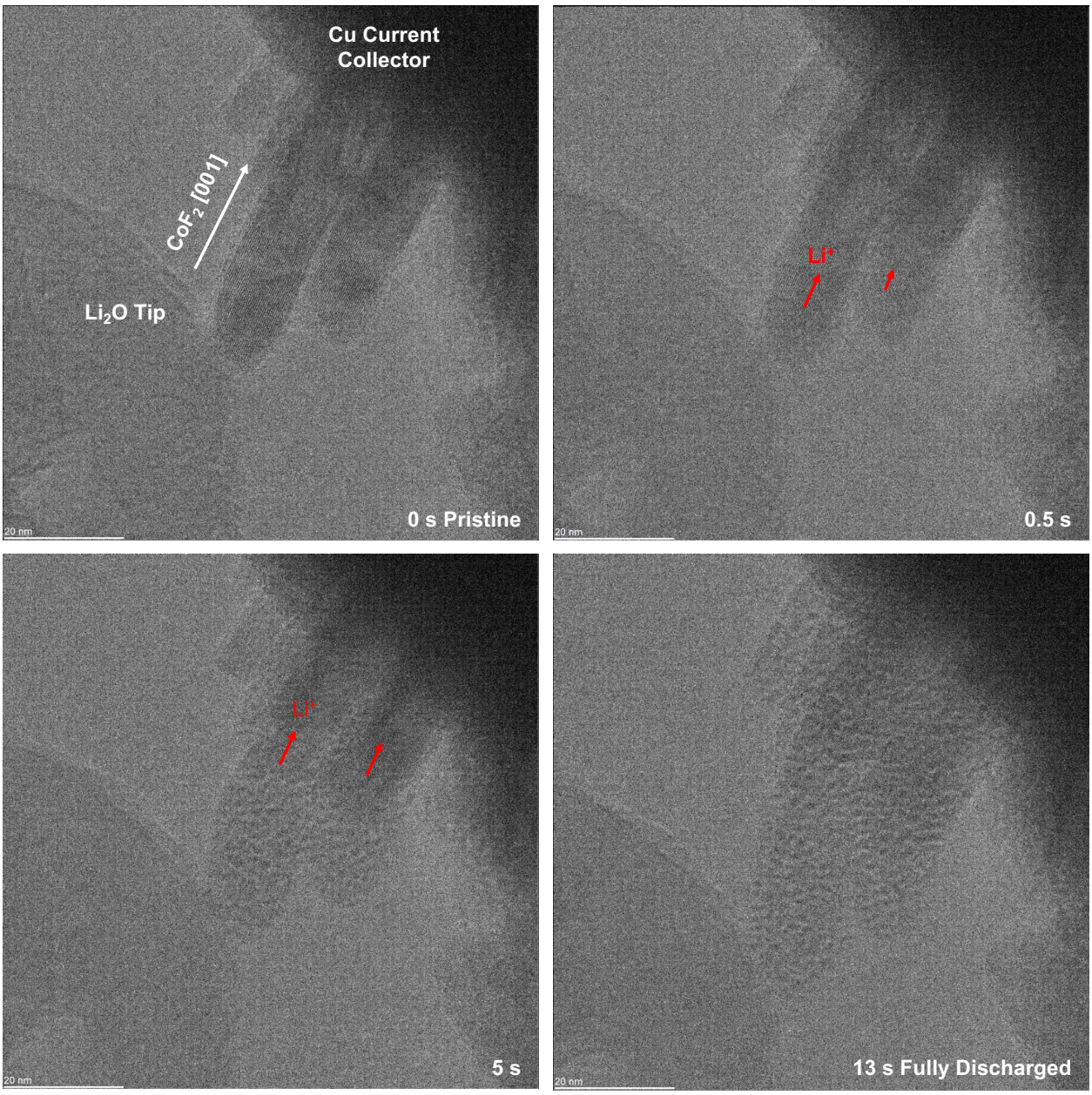

Figure S17: Visualisation of Lithiation using *in situ* TEM. BF TEM images extracted from an *in situ* TEM video, revealing the structural changes during lithiation in real-time. Structural changes follow the *ex situ* observations, where Li^+ is inserted into the CoF_2 lattice, causing the disordering of the lattice. Further lithiation leads to nucleation of Co nanoparticles in LiF matrix, until the entire nanorod is fully converted.

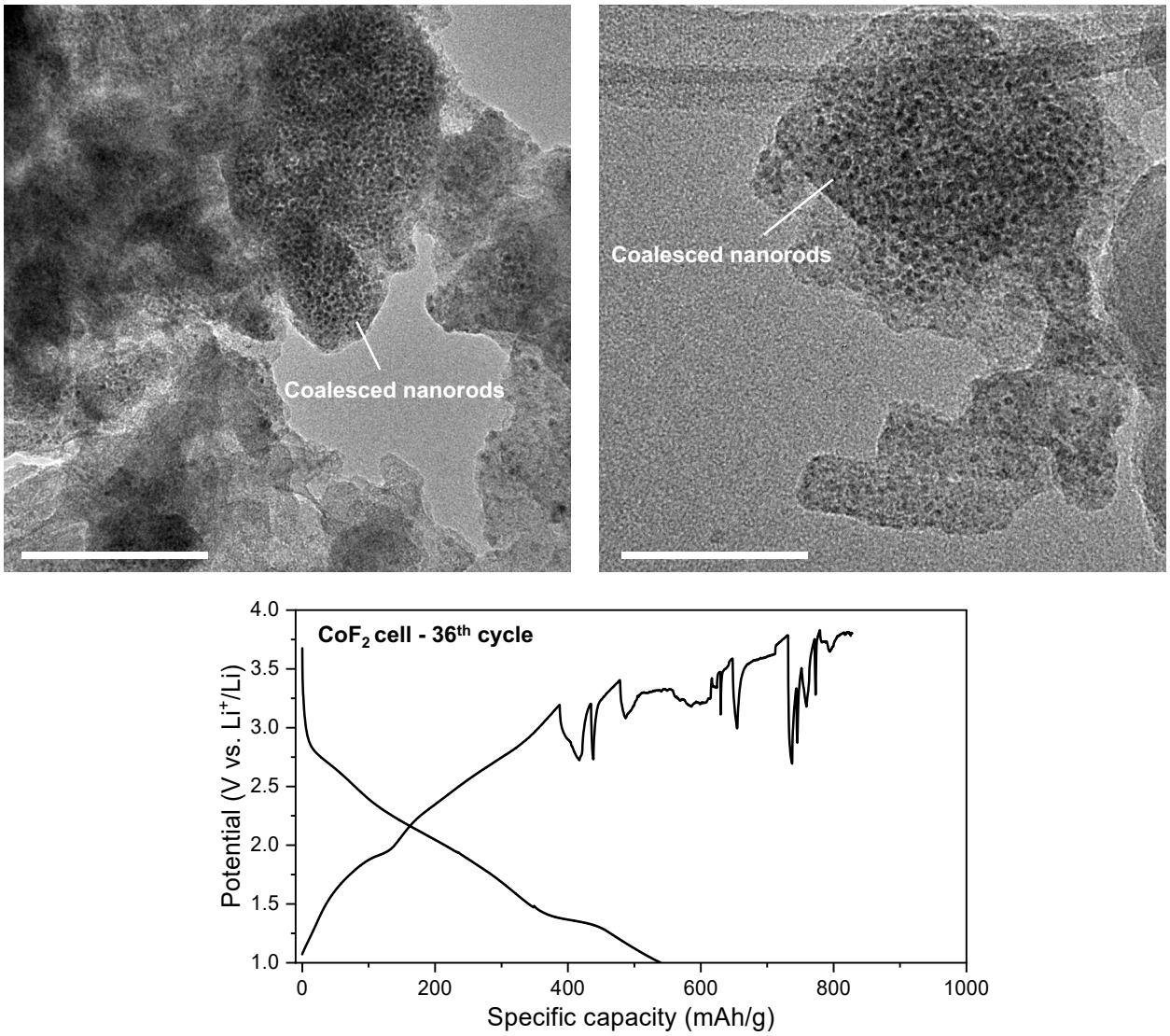

Figure S18: CoF_2 nanorods after extended cycling. Top: coalescence of multiple CoF_2 nanorods observed after 30 cycles. Scale bar = 100 nm. Bottom: the galvanostatic profile of the 36th cycle of a CoF_2 nanorod cell.

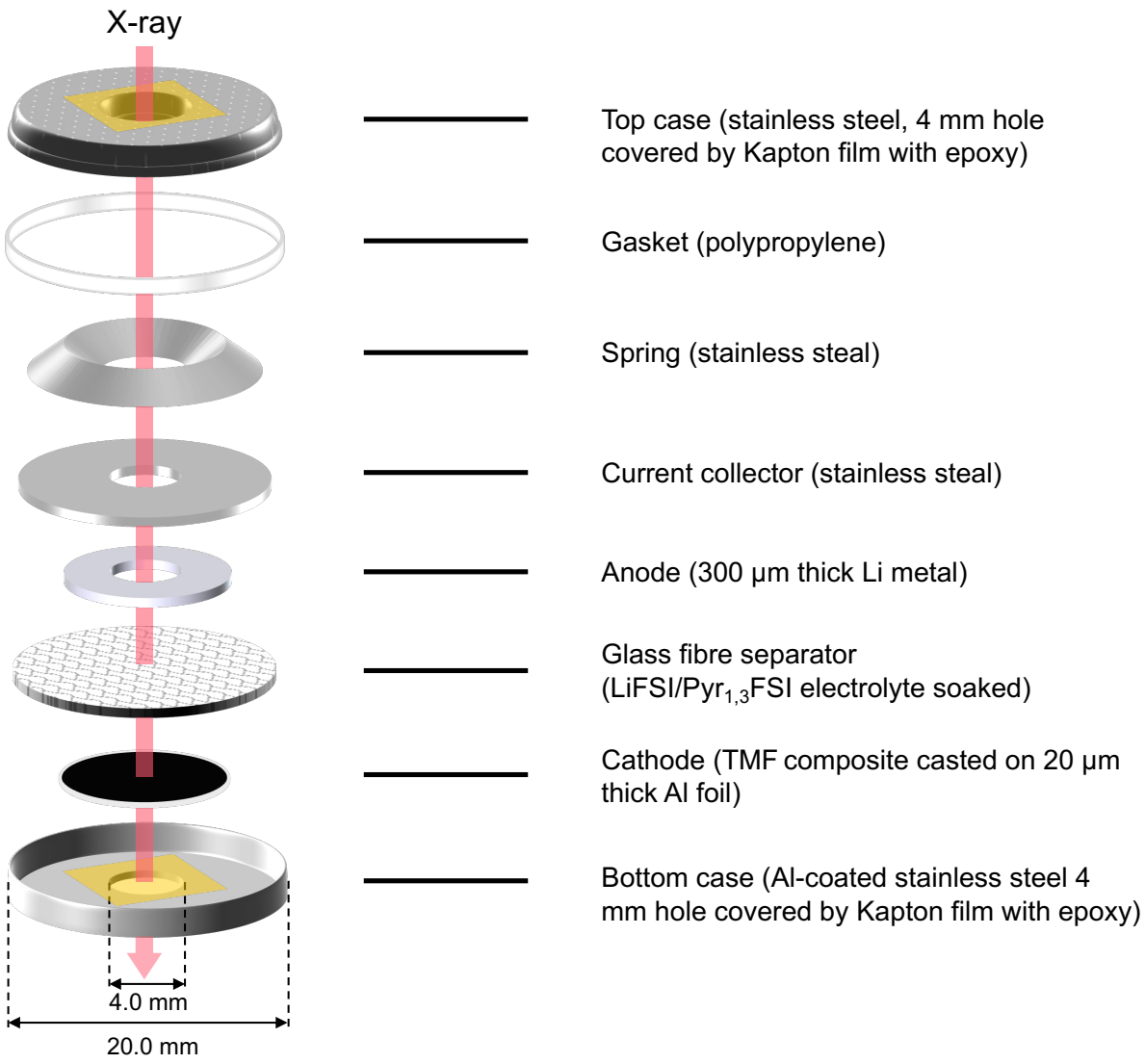

Figure S19: Configuration of the coin cell setup used for the *operando* XRD experiment. A 4 mm-diameter hole was drilled through all cell components except the CoF_2 nanorod cathode and the electrolyte-soaked separator, enabling X-ray transmission while maintaining efficient ion transport and avoiding short-circuiting. The holes in the top and bottom cases were sealed externally with Kapton film and epoxy to prevent electrolyte leakage.

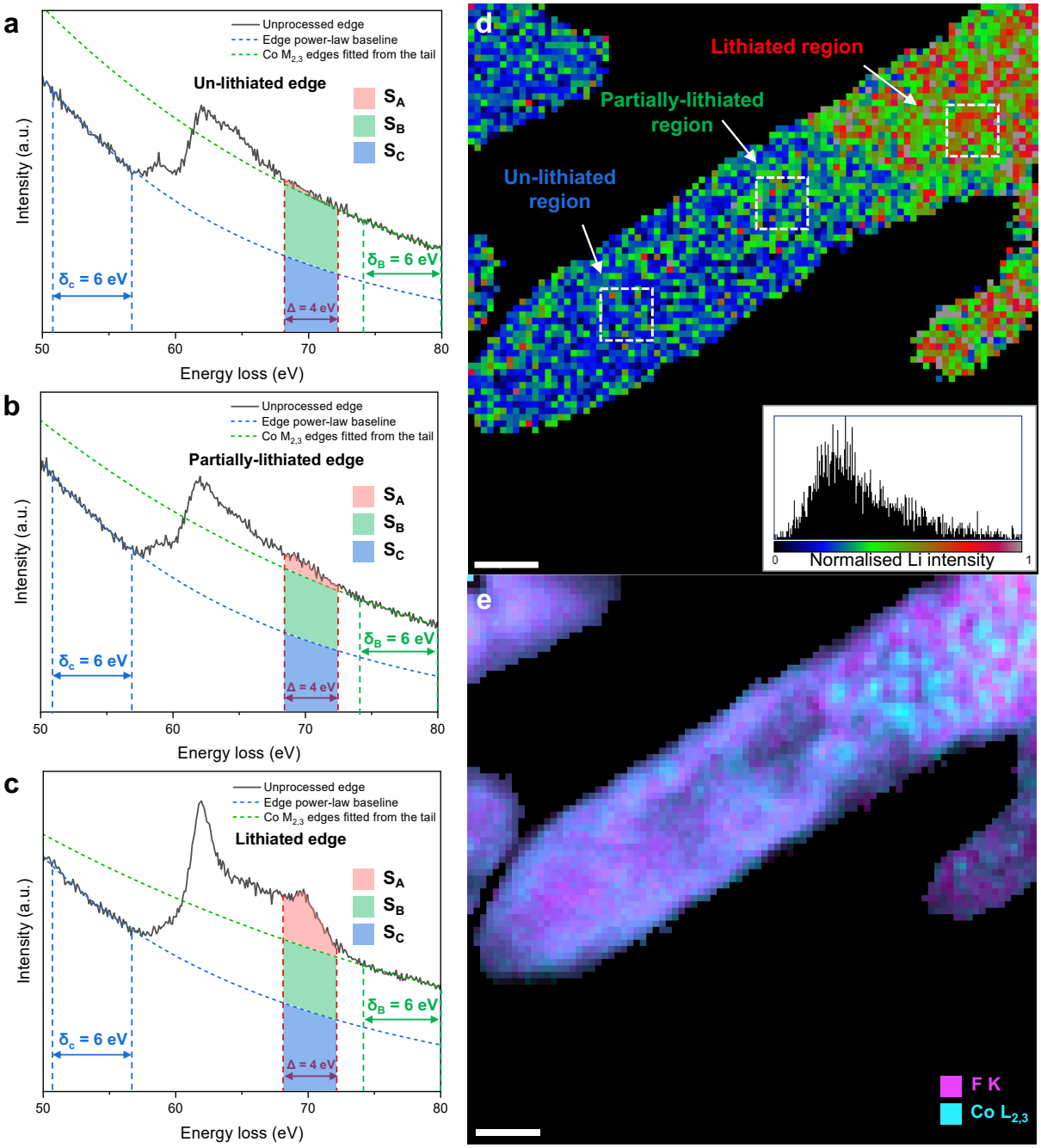

Figure S20: Li Elemental Map Generated Using the Modified S_A/S_B Method. **(a)** Spectrum of the un-lithiated region and its post-process. **(b)** Spectrum of the partially-lithiated region and its post-process. **(c)** Spectrum of the fully-lithiated region and its post-process. The power-law baseline is created from the fitting window (δ_C) of 6 eV within 51-57 eV, indicated by a blue-dashed line. The green dashed-line is the extension of the edge tail fitting in the reverse direction, which is generated based on a fitting window δ_B of 74-80 eV. **(d)** Normalised Li concentration map with the corresponding histogram, generated based on the S_A/S_B values. **(e)** Overlap of quantitative elemental maps of Co $L_{2,3}$ edges and F K edge from the high-energy loss spectrum for cross-referencing. Scale bar = 10 nm.

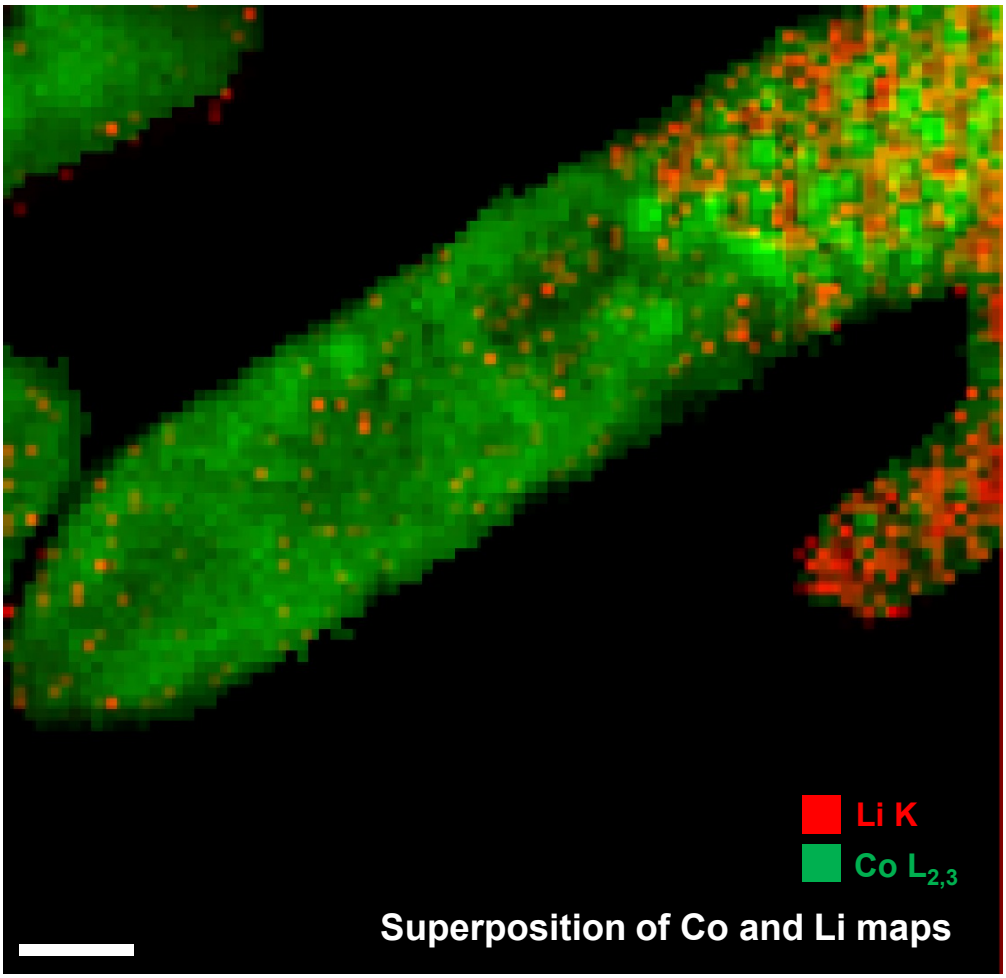

Figure S21: Superposition of the Co and Li Maps. A close match is found between the Li map generated by the S_A/S_B method and the Co map, where Li signals are found to be separated from Co signals. Scale bar = 10 nm.